Research Article | Vol. 33, No. 12 / 16 Jun 2025 / Optics Express 24303
Optics EXPRESS

Prospects of low-phonon energy Ho:MF_2 (M = Ca, Sr, Ba) crystals for 2-3 µm lasers

Ngoc Quynh Hoa Nguyen,[1] Pavel Loiko,[1] Abdelmjid Benayad,[1] Elena Dunina,[2] Liudmila Fomicheva,[3] Alexey Kornienko,[2,4] Patrice Camy,[1] and Alain Braud[1,*]

[1]Centre de Recherche sur les Ions, les Matériaux et la Photonique (CIMAP), UMR 6252 CEA-CNRS-ENSICAEN, Université de Caen Normandie, 6 Boulevard Maréchal Juin, 14050 Caen Cedex 4, France
[2]Vitebsk State Technological University, 210035 Vitebsk, Belarus
[3]Belarusian State University of Informatics and Radioelectronics, 6 Brovka St., 220027 Minsk, Belarus
[4]Vitebsk State University named after P. M. Masherov, 33 Moskovskaya Ave., 210035 Vitebsk, Belarus
*alain.braud@ensicaen.fr

Abstract: We report on a comparative spectroscopic study of Ho^{3+}-doped fluorite-type crystals MF_2 (where M stands for Ca, Sr, and Ba), regarding their applications in lasers emitting at 2 to 3 µm. The transition intensities of Ho^{3+} ions are determined within a modified Judd-Ofelt analysis accounting for configuration interaction. The stimulated-emission cross-sections for the $^5I_7 \rightarrow {}^5I_8$ (at 2.1 µm) and $^5I_6 \rightarrow {}^5I_7$ (at 2.9 µm) are determined and compared with the reference Ho:$LiYF_4$ crystal. Effects related to electron-phonon interaction are studied: i) the multiphonon sidebands responsible for long-wave emission far beyond 2 µm are observed; ii) the rates of multiphonon non-radiative relaxation from the $^5I_5$, $^5I_6$ and $^5I_7$ Ho^{3+} manifolds are computed and linked to the phonon spectra of MF_2 crystals, and iii) the parameters of phonon-assisted energy-transfer upconversion from the $^5I_7$ level are quantified using the Burshtein model. Owing to their low phonon energy behavior and inhomogeneously broadened spectral bands, Ho:MF_2 crystals are promising for broadly tunable and mode-locked lasers.

Published by Optica Publishing Group under the terms of the Creative Commons Attribution 4.0 License. Further distribution of this work must maintain attribution to the author(s) and the published article's title, journal citation, and DOI.

1. Introduction

Currently, there is a growing interest in laser sources directly emitting coherent radiation in the mid-infrared spectral range, in the so called molecular fingerprint region as it contains multiple characteristic vibrational absorption lines of atmospheric and bio molecules [1]. The use of broadly emitting laser materials is desired as they could support a broadband tuning of the laser emission and ultrashort pulse generation [2,3]. Mid-infrared lasers are relevant for applications both in industry and fundamental research, including remote sensing, molecular spectroscopy using frequency combs, supercontinuum generation, laser surgery and biomedicine.

Rare-earth ion doped crystals and glasses can serve as a versatile tool for addressing specific spectral ranges in the mid-infrared [4,5]. When laser action at long wavelength is targeted, one of the main considerations for the choice of the host material concerns its phonon spectrum [6,7]. This is determined by the energy gap law stating that the rate of multiphonon non-radiative (NR) relaxation becomes almost negligible as compared to the rate of radiative transitions if the energy gap to the lower-lying state ΔE is sufficiently large as compared to the maximum phonon energy $h\nu_{ph}$ involving both Raman and infrared active phonons ($\Delta E/h\nu_{ph} >>$ 6-7) [8,9]. The phonon energy decreases in the series oxides → fluorides → selenides → chlorides → bromides,

#558443 https://doi.org/10.1364/OE.558443
Journal © 2025 Received 3 Feb 2025; revised 9 Apr 2025; accepted 10 Apr 2025; published 2 Jun 2025

Optics EXPRESS

and so does the complexity of their synthesis with the goal of obtaining laser-quality elements. Moreover, the latter materials are often hygroscopic.

Fluoride crystals and glasses are well-known laser host matrices for rare-earth doping [10,11]. They exhibit relatively low phonon energies (570 cm^{-1} for ZBLAN glass) allowing for laser operation up to ~4 μm [12]. This is coupled with a number of advantageous properties, such as i) broad range of transparency, ii) good thermal properties, iii) high solubility of rare-earth ions, iv) weak crystal-fields leading to long luminescence lifetimes and v) low synthesis temperatures. However, their elaboration requires a precise control of the synthesis atmosphere to avoid any oxygen contamination.

Among the rare-earth ions exhibiting emission in the short-wave infrared, Holmium ions (Ho^{3+}) possessing an electronic configuration of $[Xe]4f^{10}$ (with $^5I_8$ being the ground state, see Fig. 1) attract attention due to several cascade laser transitions at 2.1 μm ($^5I_7 \rightarrow {}^5I_8$) [13], 2.9 μm ($^5I_6 \rightarrow {}^5I_7$) [14] and 3.9 μm ($^5I_5 \rightarrow {}^5I_6$) [15], with the latter two being relatively poorly explored. Recently, due to a significant progress in the technology of fluoride fibers, Ho:ZrF_4 and Ho:InF_3 fiber lasers enabled the generation of high-power, wavelength tunable output in the mid-infrared [16,17]. Very recently, Boilard *et al.* reported on a Ho:InF_3 fiber laser delivering 1.7 W at 3920 nm with a slope efficiency of 9.2% versus the absorbed pump power at 888 nm [16]. Jackson developed a Ho^{3+},Pr^{3+}:ZrF_4 fiber laser generating 2.5 W at 2860 nm with a slope efficiency of 29% versus the launched pump power at 1100 nm [17].

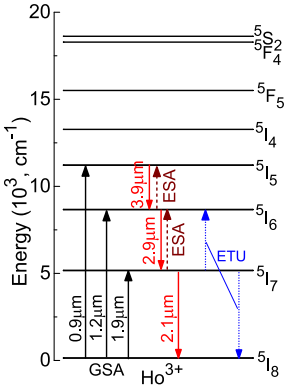


Fig. 1. A partial energy-level scheme of Ho^{3+} ions showing laser transitions in the near and mid-infrared, GSA and ESA – ground- and excited-state absorption, respectively, ETU – energy-transfer upconversion.

Ho^{3+}-doped fluoride single-crystals, such as Ho:$LiYF_4$ [18], Ho:CaF_2 [19] or Ho:BaY_2F_8 [20], appear as excellent candidates for the development of mid-infrared lasers, as they bring the advantage of high thermal conductivity potentially enabling power scaling. Ye *et al.* reported on a cascade Ho:$LiYF_4$ laser pumped at 1150 nm delivering 0.78 W at 2953 nm with a slope efficiency of 36.1% [21]. Tabirian *et al.* demonstrated room temperature pulsed laser operation of a Ho:BaY_2F_8 laser at 3.9 μm with a slope efficiency of 14.5% pumping at 890 nm [22].

Among the crystalline fluoride materials, the family of divalent-metal bifluorides MF_2, where M stands for Ca, Sr, Ba, Cd, Pb or their mixture [10,23], attracts a lot of attention for rare-earth doping [24–26]. The main feature of these materials is a multi-site behavior: at low doping levels (<0.1 at.%), several rare-earth sites with different symmetries coexist, namely, tetragonal (C_4 v) and trigonal (C_3 v) ones, with local charge compensation by interstitial F_i^- anions, and simple cubic (O_h) ones, with non-local charge compensation, and at moderately to high doping levels (≥ 0.5 at.%), the majority of the dopant ions form clusters of increasing complexity (from dimers towards agglomerates of RE^{3+} - F_i^- pairs) [27]. The latter leads to a significant

Optics EXPRESS

inhomogeneous spectral line broadening which results in a "glassy-like" spectroscopic behavior, *i.e.*, the absorption and emission spectra of rare-earth ions in MF_2 crystals resemble those in fluoride glasses. Direct imaging of simple rare earth clusters in Yb^{3+}:CaF_2 was reported [28]. Kazanski *et al.* suggested the existence of hexameric Ln_6F_{37} clusters with an inner F_{12+1} cuboctahedron, which replaces the structural unit Ca_6F_{32} with an inner F_8 cube in the fluorite crystal lattice [29]. The broad and structureless gain profiles of rare-earth ions in MF_2 crystals, coupled with very high thermal conductivity of the latter ($\kappa = 11.7$ $Wm^{-1}K^{-1}$ for undoped CaF_2), determine their relevance for ultrashort pulse generation and amplification in high-power/energy systems, as demonstrated around 1 µm [24]. In addition, the growth of MF_2 crystals is well developed, as they serve as mid-infrared optical windows and substrates.

So far, Ho^{3+}-doped CaF_2 crystals have been mostly studied for lasers emitting at 2 µm [30–32]. Very recently, Wang *et al.* reported on a Ho,Pr:CaF_2 laser pumped at 1150 nm generating 0.15 W at 2860 nm with a slope efficiency of 5% [33]. Much less attention has been paid to its Sr and Ba counterparts even though they exhibit lower phonon energies [32] consequently potentially unlocking even lasing at 3.9 µm.

In the present work, we report on a comprehensive spectroscopic study of three Ho:MF_2 crystals (with M = Ca, Sr, and Ba), regarding their stimulated-emission properties at 2 µm and 3 µm, emission lifetimes and energy-transfer upconversion.

2. Crystal growth

The Ho^{3+}-doped fluorite-type crystals, MF_2 (M = Ca, Sr and Ba), were grown by the Bridgman-Stockbarger method. The starting powders were divalent-metal fluorides CaF_2, SrF_2 and BaF_2 (purity: 4N, *Sigma-Aldrich*) and holmium fluoride, HoF_3, obtained by fluorination of holmium oxide Ho_2O_3 (purity: 4N, *Alfa Aesar*) using an excess of ammonium hydrogen bifluoride (NH_4HF_2) solution at 250 °C. The staring Ho^{3+} doping level was 0.5 at.% with respect to M^{2+} cations. The growth was performed using graphite crucibles (diameter: Ø8 mm, height: 40 mm). To avoid any oxygen contamination, the growth chamber was first sealed to vacuum ($<10^{-5}$ mbar) and refilled with a mixture of $Ar + CF_4$ gases. The precursors were well mixed and placed in the crucible which was then heated at a temperature slightly above the melting point for 2 h to homogenize the melt. The CaF_2, SrF_2, and BaF_2 compounds melt congruently at 1418 °C, 1477 °C, and 1386 °C, respectively. The crystal growth was enabled by a vertical translation of the crucible through the hot zone with a temperature gradient of 30–40 °C/cm at a rate of 1–3 mm/h. Once the growth was completed, the crystals were gradually cooled to room temperature within 72 h. No post-growth annealing was applied.

The as-grown crystals had a cylindrical shape (Ø7-8 mm, length: 35 - 40 mm) and they were transparent with a slight rose coloration associated with Ho^{3+} absorption. The crystals were free of defects and inclusions. For spectroscopic studies, we cut cylindrical samples from the central part of the boules, Fig. 2.

For comparison, 1 at.% Ho:$LiYF_4$ crystal was also grown by the Czochralski method and oriented along its $\boldsymbol{a}$-axis giving access to π and σ polarizations.

The structure of the grown crystals was confirmed by X-ray powder diffraction using a *Rigaku* diffractometer (step size: 0.01°, step time: 0.06 s). All three crystals crystallize in the cubic class (space group $Fm\bar{3}m - O_h^5$, No. 225) having a lattice constant a of 5.4565 Å, 5.7827 Å, and 6.1711 Å for M = Ca, Sr and Ba, respectively. In the fluorite-type structure, the divalent-metal cations M^{2+} are bonded in a face-centered cubic geometry to eight equivalent F^- anions.

The primitive cell of MF_2 crystals contains three nonequivalent atoms giving rise to nine phonon modes, with three of them being the acoustic ones. At the center of the Brillouin zone Γ ($\boldsymbol{k} = 0$), the group theory analysis predicts three distinct optical phonon modes, namely a doubly degenerate infrared-active TO T_{1u}, a triply degenerate Raman-active mode T_2 g, and an infrared-active nondegenerate LO T_{1u} (listed in the order of increasing phonon energy) [34]. The

Optics EXPRESS

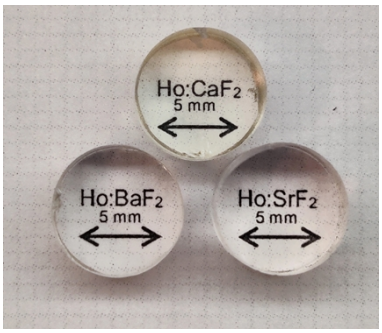


Fig. 2. A photograph of laser-grade polished samples cut from the as-grown Ho^{3+}:MF_2 crystals.

Raman spectra of Ho^{3+}:MF_2 crystals were measured using a confocal microscope (InVia Qontor, *Renishaw*) with a × 50 *Leica* objective and an Ar^+ ion laser (514 nm). In the Raman spectra, see Fig. 3(b), only one intense band is observed centered at 239.4 cm^{-1} (Ho:BaF_2), 282.3 cm^{-1} (Ho:SrF_2) and 320.1 cm^{-1} (Ho:CaF_2) with a T_2 g symmetry. The full width at half maximum (FWHM) of this band is 10.31 cm^{-1}, 9.21 cm^{-1} and 10.69 cm^{-1}, respectively. The LO phonon energy for CaF_2, SrF_2 and BaF_2 is 466 cm^{-1}, 366 cm^{-1}, and 319 cm^{-1}, respectively [35].

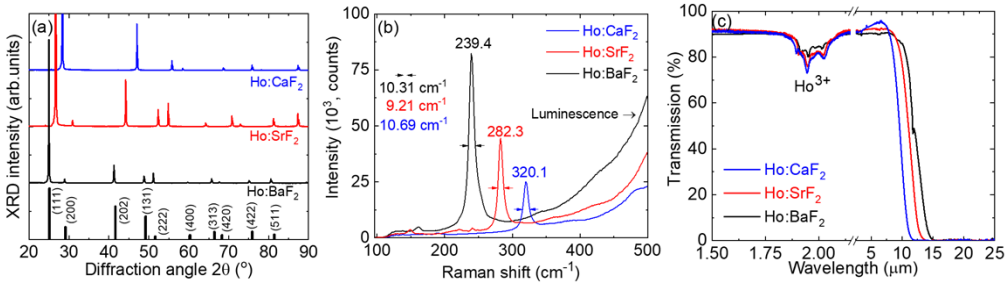


Fig. 3. Characterization of the as-grown Ho^{3+}:MF_2 crystals (M = Ca, Sr, Ba): (a) X-ray powder diffraction (XRD) patterns, *vertical bars* – theoretical reflections for undoped BaF_2, (*hkl*) – Miller's indices; (b) Raman spectra, λ_{exc} = 514 nm, *numbers* – peak frequencies and Raman peak widths (FWHM); (c) Infrared transmission spectra.

The infrared transmission spectra were measured using a *Shimadzu* Nicolet Apex FTIR spectrometer, Fig. 3(b). The IR absorption edge for the studied crystals is 14.17 μm (Ho:BaF_2), 12.66 μm (Ho:SrF_2) and 10.92 μm (Ho:CaF_2) being close to that for undoped materials.

3. Optical spectroscopy

3.1. Optical absorption

The absorption spectra of Ho^{3+} ions in MF_2 crystals were measured using a spectrophotometer (*Varian* CARY 5000) with a spectral resolution of 0.4 nm to 1.5 nm, depending on the spectral range. The absorption bands in the transparency range are related to $4f - 4f$ electronic transitions of Ho^{3+} ion from its ground state, $^5I_8$. The UV absorption edge for the studied crystals is found at <200 nm (Ho:CaF_2), 210 nm (Ho:SrF_2) and 214 nm (Ho:BaF_2). The MF_2 crystals exhibit a very broad bandgap E_g in the range of 11–12 eV [36]. For each crystal, the absorption cross-sections, $\sigma_{abs} = \alpha_{abs}/N_{Ho}$, were calculated from the absorption coefficient α_{abs} and ion density N_{Ho}. The latter was estimated using the segregation coefficients of Ho^{3+} ions, K_{Ho} = 1 (CaF_2), 0.98 (SrF_2)

Optics EXPRESS

and 0.89 (BaF_2), yielding N_{Ho} of 1.218×10^{20} at/cm^3, 1.009×10^{20} at/cm^3 and 0.732×10^{20} at/cm^3, respectively.

The σ_{abs} spectra are plotted in Fig. 4(a-f). The $4f-4f$ electronic transitions of Ho^{3+} ions were assigned according to the energy-levels of the free ion reported by Carnall *et al.* [37]. The absorption bands are broad and almost structureless due to the inhomogeneous spectral line broadening.

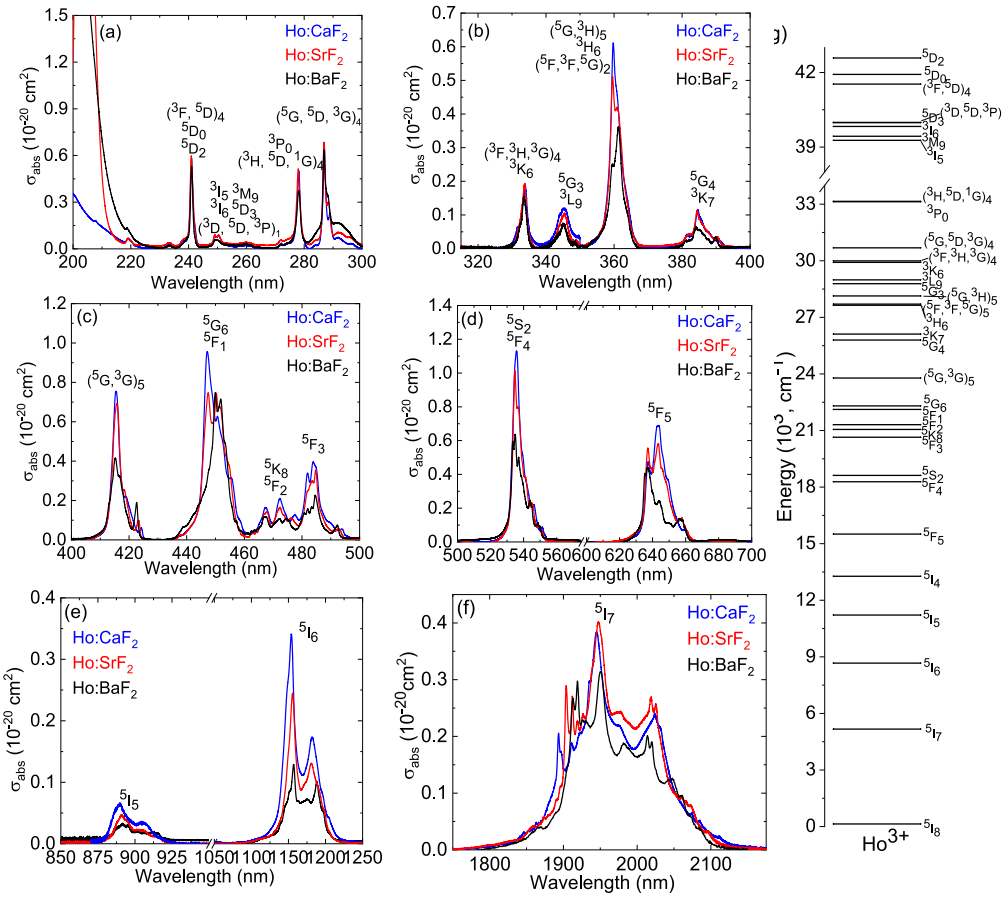


Fig. 4. (a-f) Absorption spectra of Ho^{3+}:MF_2 crystals (M = Ca, Sr, and Ba). The assignment of electronic transitions is according to Carnall *et al.* [37]; (g) the energy-level scheme of Ho^{3+} ions showing all the transitions assigned in the spectra.

The $^5I_8 \rightarrow {}^5I_7$ absorption band is used for resonant (also referred to as in-band) pumping of 2.1-μm Ho lasers enabled, *e.g.*, by Tm-fiber lasers or GaSb semiconductor laser diodes emitting at 1.94 μm [38]. For the Ho:CaF_2 crystal, the maximum σ_{abs} is 3.83×10^{-21} cm^2 at 1944.8 nm and the FWHM of the corresponding peak is ~38 nm relaxing the requirements for the choice of the pump wavelength / control of the temperature drift of the diode wavelength. The excitation of 2.9-μm Ho lasers is enabled by pumping into the $^5I_8 \rightarrow {}^5I_6$ absorption band, *e.g.*, by Raman-shifted Yb-fiber lasers operating at 1.15 μm [19]. For Ho:CaF_2, the peak σ_{abs} for this transition is 3.41×10^{-21} cm^2 at 1153.7 nm and the absorption bandwidth is ~16 nm.

In the M = Ca → Sr → Ba series, the absorption cross-sections tend to decrease due to a variation of the crystal-field strength. The spectra also become more structured. Normani *et al.*

Optics EXPRESS

Table 1. Absorption Oscillator Strengths[a] for Ho^{3+} Ions in MF_2 (M = Ca, Sr, and Ba) Crystals

Transition	Ho^{3+}:CaF_2		Ho^{3+}:SrF_2		Ho^{3+}:BaF_2	
$^5I_8 \rightarrow$	f_{exp},	f_{calc}, mJ-O	f_{exp},	f_{calc}, mJ-O	f_{exp},	f_{calc}, mJ-O
$^{2S+1}L_J$	10^{-6}	10^{-6}	10^{-6}	10^{-6}	10^{-6}	10^{-6}
$^5I_7$	1.382	$1.040^{ED} + 0.429^{MD}$	1.359	$0.962^{ED} + 0.437^{MD}$	1.107	$0.873^{ED} + 0.436^{MD}$
$^5I_6$	0.847	0.836^{ED}	0.702	0.742^{ED}	0.491	0.646^{ED}
$^5I_5$	0.207	0.164^{ED}	0.232	0.144^{ED}	0.108	0.120^{ED}
$^5F_5$	3.030	2.502^{ED}	2.683	2.341^{ED}	1.944	1.839^{ED}
$^5S_2 + {}^5F_4$	4.103	3.760^{ED}	3.423	3.138^{ED}	2.648	2.491^{ED}
$^5F_3 + {}^3D_2 + {}^3K_8 + {}^5G_6$	6.991	$6.904^{ED} + 0.092^{MD}$	6.679	$6.722^{ED} + 0.094^{MD}$	5.480	$5.373^{ED} + 0.094^{MD}$
$^5G_5$	2.482	2.552^{ED}	2.541	2.644^{ED}	1.834	1.867^{ED}
$^5G_4 + {}^3K_7$	0.536	$0.524^{ED} + 0.004^{MD}$	0.606	$0.448^{ED} + 0.004^{MD}$	0.390	$0.323^{ED} + 0.004^{MD}$
$^5G_5 + {}^3H_6$	2.408	2.335^{ED}	2.333	2.181^{ED}	1.596	1.606^{ED}
$^5G_3 + {}^3L_9$	0.769	$1.058^{ED} + 0.002^{MD}$	0.470	$0.815^{ED} + 0.002^{MD}$	0.328	$0.586^{ED} + 0.002^{MD}$
$^3F_4 + {}^3K_6$	0.613	0.893^{ED}	0.522	0.889^{ED}	0.411	0.598^{ED}
r.m.s. dev.		*0.211*		*0.192*		*0.126*

[a] f_{exp} and f_{calc} - experimental and calculated absorption oscillator strengths, respectively, ED – electric dipole, MD – magnetic dipole.

suggested that this effect can be explained by the decreasing variety of rare-earth clusters in BaF_2 as compared to SrF_2 and CaF_2 [10].

3.2. Judd-Ofelt analysis

The measured absorption spectra of Ho^{3+} ions in the MF_2 crystals were analyzed using the modified Judd-Ofelt (mJ-O) theory accounting for weak configuration interaction [39]. Within this parametrization scheme, the electric dipole (ED) line strengths for $4f - 4f$ transitions are given by [39,40]:

$$S_{\text{ff}}^{ED}(JJ') = \sum_{k=2,4,6} U^{(k)}\tilde{\Omega}_k, \tag{1a}$$

$$\tilde{\Omega}_k = \Omega_k[1 + 2\alpha(E_J - E_{J'} - 2E_f^0)], \tag{1b}$$

where the intensity parameters $\tilde{\Omega}_k$ are the linear functions of energies (E_J and $E_{J'}$) of the two multiplets participating in the optical transition $J \rightarrow J'$, E_f^0 is the mean energy of the $4f^n$ ground configuration and $\alpha \approx 1/(2\Delta)$, where Δ is the average energy difference between the ground $4f^n$ and excited $4f^{n-1}5d^1$ configurations. The set of reduced squared matrix elements $U^{(k)}$ ($k = 2$, 4, 6) for transitions in absorption and emission was calculated using the free-ion parameters reported by Carnall *et al.* [37]. The line strengths of magnetic dipole (MD) transitions (with $\Delta J = J - J' = 0, \pm 1$) were calculated separately within the Russell–Saunders approximation using Ho^{3+} wave functions under the free-ion assumption. The refractive indices of MF_2 crystals were determined from the dispersion formulas [41].

The experimental, f_{exp}, and calculated, f_{calc}, oscillator strengths for transitions of Ho^{3+} ions in absorption for the studied MF_2 crystals are listed in Table 1. The ED and MD contributions are shown. The use of the mJ-O theory allows to reduce the root mean square deviation between the

Optics EXPRESS

f_{exp} and f_{calc} values (*e.g.,* it amounts to 0.291 and 0.211 for the standard J-O theory and the mJ-O one for Ho:CaF_2). The obtained intensity parameters Ω_2, Ω_4, Ω_6 and α are listed in Table 2. In the M = Ca → Sr → Ba series, Ω_2 increases, Ω_4 and Ω_6 decrease and α decreases (or, in other words, the energy gap Δ to the excited configuration of the opposite parity progressively increases). According to Jorgensen and Reisfeld [42], the magnitude of Ω_2 reflects the information about short range coordination effects (*i.e.*, the covalency of bonds between the rare-earth dopant ion and the ligand, as well as the point symmetry of the rare-earth site), while Ω_4 and Ω_6 parameters are affected by long-range effects (in particular, Ω_6 is related to the rigidity of the medium in which the ions are accommodated).

Table 2. Intensity Parameters of Ho^{3+} Ions in MF_2 Crystals

Host crystal	Ω_2, 10^{-20} cm^2	Ω_4, 10^{-20} cm^2	Ω_6, 10^{-20} cm^2	α, 10^{-4} cm	Δ, 10^4 cm
Ho^{3+}:CaF_2	0.260	3.717	3.584	0.062	8.1
Ho^{3+}:SrF_2	0.333	3.341	2.407	0.048	10.4
Ho^{3+}:BaF_2	0.388	1.917	1.451	0.018	27.8

Using the intensity parameters derived from the absorption spectra, we calculated the probabilities of spontaneous radiative transitions of Ho^{3+} ions. For the sake of brevity, in Table 3, we list only the parameters relevant for laser operation in the near- and mid-infrared, namely, the radiative lifetimes τ_{rad} of the $^5I_7$ to $^5I_6$ states, and the luminescence branching ratios $\beta_{JJ'}$ for the $^5I_6 \rightarrow {}^5I_7$ and $^5I_5 \rightarrow {}^5I_6$ transitions. In the M = Ca → Sr → Ba series, the radiative lifetimes for all the three considered excited states increase, namely, from 16.89 ms to 18.39 ms ($^5I_7$) and from 7.74 ms to 9.25 ms ($^5I_6$). This agrees well with the gradual drop of the absorption oscillator strengths for transitions to these excited states. The luminescence branching ratios for the transitions giving rise to mid-infrared emission at 2.9 μm and 3.9 μm also gradually increase.

Table 3. Selected Probabilities[a] of Spontaneous Radiative Transitions of Ho^{3+} in MF_2 crystals

Host crystal	$\tau_{rad}(^5I_7)$, ms	$\tau_{rad}(^5I_6)$, ms	$\tau_{rad}(^5I_5)$, ms	$\beta_{JJ'}(^5I_6 \longrightarrow {}^5I_7)$, %	$\beta_{JJ'}(^5I_5 \longrightarrow {}^5I_6)$, %
Ho^{3+}:CaF_2	16.89	7.74	8.42	15.7	7.5
Ho^{3+}:SrF_2	17.14	8.13	9.16	17.1	8.3
Ho^{3+}:BaF_2	18.39	9.25	11.55	17.8	8.4

[a] τ_{rad} – radiative lifetime, $\beta_{JJ'}$ – luminescence branching ratio.

3.3. Stimulated-emission cross-sections

The luminescence of Ho^{3+} ions at 2 μm (the $^5I_7 \rightarrow {}^5I_8$ transition) and 3 μm (the $^5I_6 \rightarrow {}^5I_7$ transition) was excited by a Ti:Sapphire laser (Spectra Physics, Model 3900S) tuned to 890 nm and collected using an uncoated CaF_2 lens, a ZrF_4 fiber (*Thorlabs*) and detected with an optical spectrum analyzer (OSA, *Yokogawa* AQ6376) with a resolution of 2 nm. The OSA was purged with N_2 gas to eliminate the structured absorption of water vapor in the atmosphere. The set-up was calibrated using a 20 W quartz iodine lamp. For polarized measurements, a metal grid polarizer (*Thorlabs*) was employed.

The stimulated-emission (SE) cross-sections, σ_{SE}, were calculated using the Füchtbauer-Ladenburg formula [43]:

$$\sigma_{SE}(\lambda) = \frac{\lambda^5}{8\pi n^2 \tau_{rad} c} \frac{\beta_{JJ'} I(\lambda)}{\int \lambda I(\lambda) d\lambda}, \quad (1)$$

where λ is the wavelength of light, n is the refractive index, c is the speed of light, τ_{rad} is the radiative lifetime of the emitting state ($^5I_7$ or $^5I_6$), $\beta_{JJ'}$ is the luminescence branching ratio, being

Optics EXPRESS

determined via the Judd-Ofelt theory, and $I(\lambda)$ is the measured luminescence spectral profile for the considered transition calibrated for the apparatus function.

The σ_{SE} spectra of Ho^{3+} ions in MF_2 and $LiYF_4$ crystals around 2 μm and 3 μm are shown in Fig. 5. The spectra of fluorite-type crystals present a significant broadening due to the ion clustering, spanning from 1.85 to 2.2 μm and 2.7 to 3.1 μm, respectively. In the M = Ca → Sr → Ba, the emission bands become narrower due to the change in the crystal field strength [10]. For the $^5I_7 \rightarrow {}^5I_8$ transition of Ho^{3+} ions in CaF_2, the maximum σ_{SE} reaches 0.54×10^{-20} cm^2 at 2024.8 nm, while σ_{SE} amounts to 0.22×10^{-20} cm^2 at 2084nm which lies in the expected laser spectral range because of the quasi-3-level nature of the laser transition. In the M = Ca → Sr → Ba series, the SE cross-sections decrease mainly because of the longer radiative lifetime of the $^5I_7$ manifold. For the $^5I_6 \rightarrow {}^5I_7$ transition for Ho:CaF_2, σ_{SE} reaches 0.89×10^{-20} cm^2 at 2847.2 nm and the emission bandwidth (FWHM) is as broad as ~73 nm.

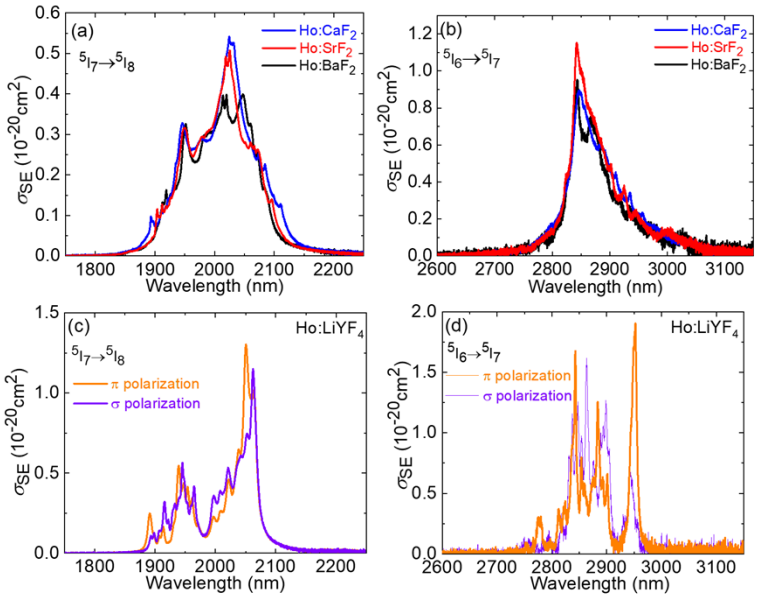


Fig. 5. (a-d) Stimulated-emission (SE) cross-section, σ_{SE}, spectra of Ho^{3+} ions in fluoride crystals: (a,c) the $^5I_7 \rightarrow {}^5I_8$ transition at ~2 μm; (b,d) the $^5I_6 \rightarrow {}^5I_7$ transition at ~2.9 μm. (a,b) MF_2 (M = Ca, Sr, and Ba) crystals; (c,d) $LiYF_4$ crystal, π and σ light polarizations.

Table 4 summarizes the data on the absorption and stimulated-emission cross-sections of Ho^{3+} ions in MF_2 crystals for the relevant pump and laser wavelengths.

For the reference ordered Ho:$LiYF_4$ crystal, the peak SE cross-sections are higher measuring 1.30×10^{-20} cm^2 at 2050.7 nm ($^5I_7 \rightarrow {}^5I_8$) and 1.91×10^{-20} cm^2 at 2952.3 nm ($^5I_6 \rightarrow {}^5I_7$) for π-polarized light at the expense of much narrower emission bandwidths (~25 nm and ~13 nm, respectively).

2-μm Ho lasers operate on a quasi-3-level scheme due to the inherent laser reabsorption from the ground-state. Thus, gain cross-sections, $\sigma_{gain} = \sigma_{SE} \times \beta - \sigma_{abs} \times (1 - \beta)$, are calculated to investigate the gain bandwidth and the expected laser wavelength, where $\beta = N_2(^5I_7)/N_{Ho}$ is the population inversion ratio. The spectral gain profiles for Ho:CaF_2 at 2 μm are shown in Fig. 6(a). On increasing β from 0.2 to 0.4, the spectral gain maximum experiences a blue shift from 2110 nm to 2033nm. The gain bandwidth (FWHM) for an intermediate β of 0.35 reaches 95 nm. This value is superior to those for Ho:SrF_2 (72 nm) and Ho:BaF_2 (64 nm), Fig. 6(b).

Optics EXPRESS

Table 4. Absorption and Emission Characteristics[a] of Ho^{3+}:MF_2 Crystals

Parameter / Crystal	Ho:CaF_2		Ho:SrF_2		Ho:BaF_2	
	$^5I_8 \rightarrow {}^5I_7$	$^5I_8 \rightarrow {}^5I_6$	$^5I_8 \rightarrow {}^5I_7$	$^5I_8 \rightarrow {}^5I_6$	$^5I_8 \rightarrow {}^5I_7$	$^5I_8 \rightarrow {}^5I_6$
λ_{abs}, nm	1944.8	1153.7	1947.6	1155.6	1950.4	1157.0
σ_{abs}, 10^{-21} cm^2	3.83	3.41	4.02	2.45	3.14	1.29
	$^5I_7 \rightarrow {}^5I_8$	$^5I_6 \rightarrow {}^5I_7$	$^5I_7 \rightarrow {}^5I_8$	$^5I_6 \rightarrow {}^5I_7$	$^5I_7 \rightarrow {}^5I_8$	$^5I_6 \rightarrow {}^5I_7$
λ_{em}, nm	2024.8	2847.2	2025.5	2842.5	2019.6	2843.8
σ_{SE}, 10^{-21} cm^2	5.43	8.94	5.08	11.52	3.99	9.53
$\Delta\lambda_{em}$, nm	121.41	72.78	134.64	55.93	134.04	59.27
$<\tau_{lum}>$, ms	15.21	3.41	16.91	5.03	18.05	5.53

[a] λ_{abs} – peak absorption wavelength, σ_{abs} – absorption cross-section, $\Delta\lambda_{abs}$ – absorption bandwidth; λ_{em} – peak emission wavelengths, σ_{SE} – stimulated emission cross-sections, $<\tau_{lum}>$ – average luminescence lifetime.

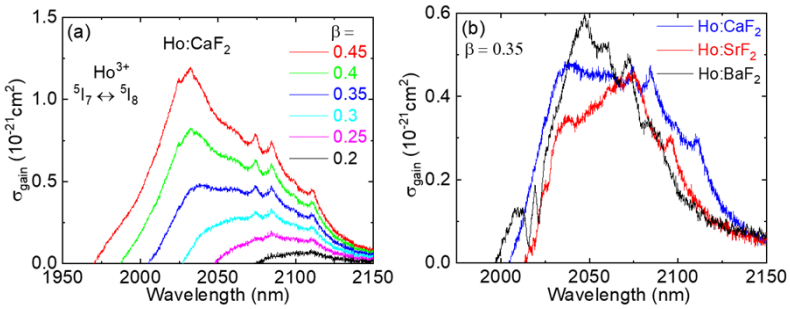


Fig. 6. (a) Gain cross-section spectra, $\sigma_{gain} = \sigma_{SE} \times \beta - \sigma_{abs} \times (1 - \beta)$, of Ho^{3+} ions in CaF_2 crystal around 2 μm plotted for different population inversion ratios (β); (b) comparison of gain profiles of Ho:MF_2 crystals (M = Ca, Sr and Ba) for a fixed $\beta = 0.35$.

The broadband gain properties of Ho:MF_2 crystals around 2 μm and 3 μm suggest their suitability for generation and amplification of femtosecond pulses at these wavelengths.

The operation of 3-μm Ho lasers is affected by the resonant excited-state absorption (ESA) from the long-living terminal laser level, $^5I_7 \rightarrow {}^5I_6$. Its cross-section, σ_{ESA}, can be calculated using the reciprocity method (McCumber relation) [20]:

$$\sigma_{ESA}(\lambda) = \sigma_{SE}(\lambda)\frac{Z_u}{Z_l}\exp\left[\frac{(hc/\lambda) - E_{ZPL}}{kT}\right] \quad (2)$$

where h is the Planck constant, k is the Boltzmann constant, T is temperature, E_{ZPL} is the zero-phonon line (ZPL) energy measured between the two lower-lying Stark sub-levels of the two involved multiplets, and Z_u and Z_l are the partition functions for the upper and lower manifolds, respectively. As the crystal-field splitting cannot be easily determined for ion clusters in fluorite type crystals, we used the data previously reported for C_4 v symmetry sites in Ho:CaF_2 [44]. In this way, we obtain $Z_u = 9.26$, $Z_l = 11.24$, and $E_{ZPL} = 3494\ cm^{-1}$ (2862 nm). For Ho:$LiYF_4$ [45], a similar calculation yields $Z_u = 10.78$, $Z_l = 11.46$ and $E_{ZPL} = 3516\ cm^{-1}$ (2843 nm). The σ_{ESA} spectra are shown in Fig. 7. ESA from the metastable $^5I_7$ state will force the Ho lasers to operate at the long-wavelength part of the emission spectrum, similarly to the quasi-3-level behavior. Indeed, in previous works on 3-μm laser operation of Ho^{3+}-doped fluorides, the laser wavelengths were 2860 nm and 2885 nm (for Ho:CaF_2 [33]) and 2953 nm (for Ho:$LiYF_4$ [21]), aligning well with the emission spectra reported in this work.

Optics EXPRESS

3.4. Phonon sidebands and energy-transfer upconversion

In this Section, we quantify energy-transfer upconversion (ETU) in Ho^{3+}-doped MF_2 crystals, ${}^5I_7 + {}^5I_7 \rightarrow {}^5I_6 + {}^5I_8$. Since this energy transfer depopulates the ${}^5I_7$ emitting laser level, it has a negative impact on the performance of 2-μm Ho lasers leading to an increased laser threshold and stronger heat loading [46,47]. At the same time, this ETU could play a positive role in preventing the bottleneck effect for 3-μm Ho lasers. Thus, it is important to quantify ETU in Ho^{3+}-doped laser materials.

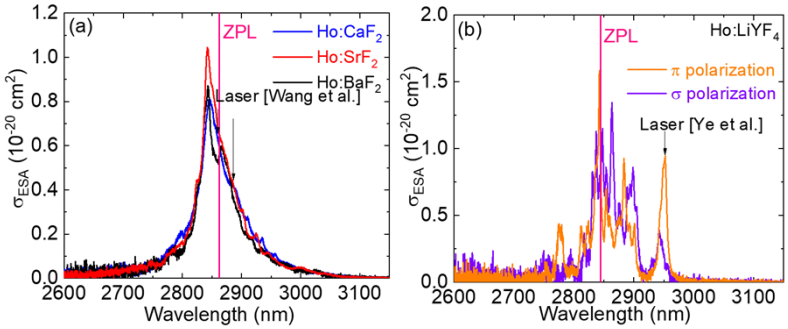


Fig. 7. Excited-state absorption (ESA) cross-section, σ_{ESA}, spectra of Ho^{3+} ions in fluoride crystals at ~3 μm. (a) MF_2 (M = Ca, Sr, and Ba) crystals; (b) $LiYF_4$ crystal, π and σ light polarizations, *vertical lines* correspond to zero-phonon line energy.

This ETU mechanism is a phonon-assisted process. Consequently, we first focus our attention on the description of the phonon sidebands of optical transitions of Ho^{3+} ions. Figure 8 presents the SE cross-section spectra for the ${}^5I_7 \rightarrow {}^5I_8$ transition of Ho^{3+} in MF_2 crystals plotted in a semi-log scale over the spectral range of 2075–2400 nm. The crystal-field splitting for Ho^{3+} ions forming clusters cannot be easily derived, still, we unambiguously assign the sharp peaks at 2113 nm ($Ho:CaF_2$), 2096nm ($Ho:SrF_2$) and 2086nm ($Ho:BaF_2$) to electronic transitions. The emission at longer wavelengths represents the phonon sideband (Stokes processes with generation of phonons). It is well described by the exponential law [32,33,48,49]:

$$\sigma_S = \sigma_0 \exp(-\alpha_S \Delta E) \tag{3a}$$

$$\sigma_{AS} = \sigma_0 \exp(-\alpha_{AS} \Delta E) \tag{3b}$$

where ΔE is the energy mismatch between the vibronic and the purely electronic transition, σ_0 is the transition cross-section at the photon energy of the electronic transition and the Stokes, α_S, and anti-Stokes, α_{AS}, material-dependent factors are given by [32]:

$$\alpha_S = (h\nu_{ph})^{-1} \{ln [\langle N \rangle / (S_0 (\langle n \rangle + 1)] - 1\} \tag{4a}$$

$$\alpha_{AS} = \alpha_S + 1/(kT) \tag{4b}$$

where, $h\nu_{ph}$ is the maximum phonon energy, $<N>$ is the average number of phonons involved in the transition, S_0 is the Pekar-Huang-Rhys coupling constant and $<n>$ is the phonon occupation number.

Figure 8 presents the fits of the exponential phonon sidebands of Ho^{3+} ions with Eq. (3a) yielding the following material constants: $\alpha_S = 7.0 \times 10^{-3}$ cm (CaF_2), 7.2×10^{-3} cm (SrF_2), and 7.9×10^{-3} cm (BaF_2). The increase of the α_S constant is in line with the decreasing phonon energy in the M = Ca → Sr → Ba series.

Optics EXPRESS

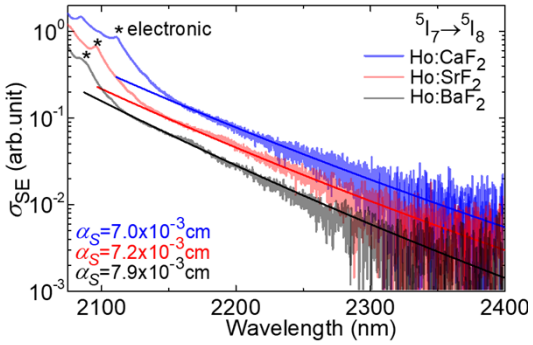


Fig. 8. Long-wave multi-phonon sidebands from the $^5I_7 \rightarrow {}^5I_8$ transition of Ho^{3+} ions in MF_2 (M = Ca, Sr, and Ba) crystals.

The ETU rate was evaluated using the hopping (Burshtein) model of migration assisted energy transfer [50]. The macroscopic ETU rate was calculated as [51,52]:

$$W_{ETU} = \pi\left(\frac{2\pi}{3}\right)^{5/2}\sqrt{C_{DD}C_{DA}}N_{Ho}^2 \tag{5}$$

where N_{Ho} is the Ho^{3+} ion density, D and A indicate the donor and the acceptor, respectively, C_{DD} is the microparameter associated with the energy transfer among donors, the D-D process responsible for energy migration (EM), and C_{DA} is that of the D-A process, responsible for the phonon-assisted "direct" ETU, Fig. 9(a). The microparameters C_{DD} and C_{DA} are calculated from the overlap integrals between the cross-section spectra of the involved processes: stimulated-emission (SE), $^5I_7 \rightarrow {}^5I_8$, ground-state absorption (GSA), $^5I_8 \rightarrow {}^5I_7$, and excited-state absorption (ESA), $^5I_7 \rightarrow {}^5I_6$ [51,52]:

$$C_{DD} = \frac{3c}{8\pi^4 n^2}\int \sigma_{SE}(\lambda)\sigma_{GSA}(\lambda)d\lambda \tag{6a}$$

$$C_{DA} = \frac{3c}{8\pi^4 n^2}\int \sigma_{ESA}(\lambda)\sigma_{SE}(\lambda)d\lambda \tag{6b}$$

where, c the speed of light, n the refractive index, and λ is the light wavelength. In this calculation, we accounted for the Stokes multi-phonon sidebands of the SE and ESA spectra, as shown in Fig. 9(b) in the case of Ho:CaF_2.

For the latter material, our calculation gives $C_{DD} = 3.89 \times 10^{-39}$ cm^6s^{-1} and $C_{DA} = 3.40 \times 10^{-43}$ cm^6s^{-1}. Their ratio, $C_{DA} << C_{DD}$, justifies the use of the Burshtein model as the "direct" ETU (a phonon-assisted process) is much less probable than the energy migration. The concentration dependence of the macroscopic ETU rate on the rare-earth ion density could be expressed as [53]:

$$W_{\mathrm{ETU}} = K_{\mathrm{ETU}}N_{Ho} = C_{\mathrm{ETU}}N_{\mathrm{Ho}}^2, \tag{7}$$

where K_{ETU} and C_{ETU} are the concentration-dependent and independent ETU parameters, respectively.

The comparison between Eqs. (6) and (7) shows that:

$$C_{ETU} = \pi\left(\frac{2\pi}{3}\right)^{5/2}\sqrt{C_{DD}C_{DA}}, \tag{8}$$

Using the C_{DD} and C_{DA} values found earlier, we calculated $C_{ETU} = 9.68 \times 10^{-40}$ cm^6s^{-1} (for Ho:CaF_2).

Optics EXPRESS

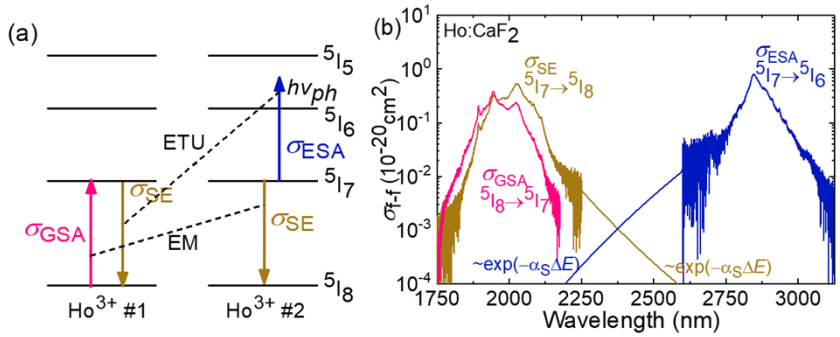


Fig. 9. (a) Illustration of the ETU mechanism: energy migration (EM) and "direct" ETU; (b) ESA ($^5I_7 \rightarrow {}^5I_6$), GSA ($^5I_8 \rightarrow {}^5I_7$) and SE ($^5I_7 \rightarrow {}^5I_8$) cross-section spectra with the multi-phonon sidebands plotted in the semi-log scale for Ho:CaF_2.

Table 5 summarizes the ETU parameters found in the different studied crystals. In the series M = Ca → Sr → Ba, the ETU rate W_{ETU} gradually decreases due to i) the weakening of the crystal-field strength and ii) the decrease of the maximum phonon energy reflected in the α_S constants.

Table 5. ETU Parameters for 0.5 at.% Ho^{3+}-doped Fluorite-Type Crystals

Crystal	N_{Ho}, 10^{20} cm^{-3}	C_{DA}, 10^{-43} cm^{6}s^{-1}	C_{DD}, 10^{-39} cm^{6}s^{-1}	C_{ETU}, 10^{-40} cm^{6}s^{-1}	K_{ETU}, 10^{-20} cm^{6}s^{-1}	W_{ETU}, s^{-1}
Ho^{3+}:CaF_2	1.218	6.10	3.89	9.68	11.79	14.36
Ho^{3+}:SrF_2	1.009	2.26	4.11	6.08	6.13	6.19
Ho^{3+}:BaF_2	0.732	1.94	2.90	4.73	3.46	2.54
Ho^{3+}:$LiYF_4$	1.380	116.89	17.17	89.34	123.29	170.43

3.5. *Luminescence lifetimes and non-radiative relaxation*

For the luminescence decay studies, we employed a setup consisting of a ns optical parametric oscillator (Horizon, *Continuum*), a 1/4 m monochromator (*Oriel* 77200), an InGaAs detector coupled to a preamplifier (bandwidth: 1.8 MHz, DHPCA-100, *FEMTO*) and an 8 GHz digital oscilloscope (DSA70804B, *Tektronix*). To avoid the effect of reabsorption (radiation trapping), the crystal samples were ground to fine powders.

The measured luminescence decay curves from the $^5I_5$, $^5I_6$ and $^5I_7$ manifolds of Ho^{3+} ions in 0.5 at.% Ho:MF_2 crystals are plotted in Fig. 10(a-c) in a semi-log scale. The excitation and detection wavelength are also given on each graph. In Fig. 10(b,c), we also show the decay curves for the 1 at.% Ho:$LiYF_4$ crystal studied for comparison. The obtained luminescence lifetimes τ_{lum} are summarized in Table 6. In the same table, we also list the corresponding radiative lifetimes τ_{rad} obtained by the Judd-Ofelt theory, the luminescence quantum efficiency $\eta_q = \tau_{lum}/\tau_{rad}$, and the ratio $\Delta E/h\nu_{ph}$, where ΔE is the energy-gap to the lower-lying manifold, and $h\nu_{\text{ph}}$ is the maximum phonon energy of the host (determined by the IR phonons for MF_2 crystals). Furthermore, for each excited state and crystal host, we calculate the rate of multiphonon non-radiative (NR) relaxation W_{NR}:

$$W_{NR} = \frac{1}{\tau_{lum}} - \frac{1}{\tau_{rad}}. \tag{9}$$

Optics EXPRESS

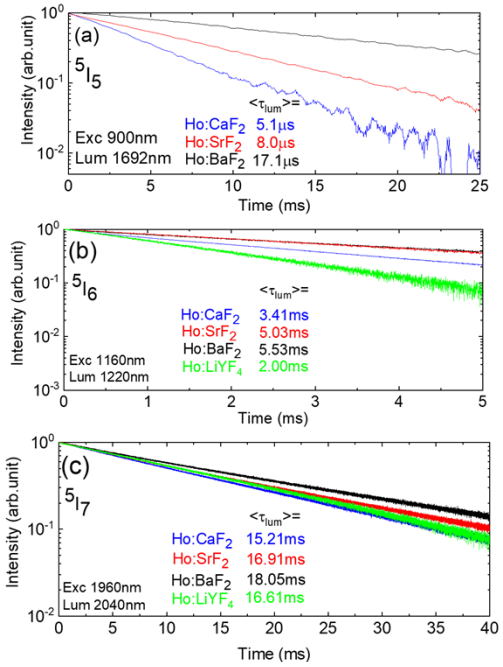


Fig. 10. (a-c) Luminescence decay curves from (a) $^5I_5$, (b) $^5I_6$ and (c) $^5I_7$ Ho^{3+} manifolds in 0.5 at.% Ho:MF_2 crystals (M = Ca, Sr, and Ba) measured under resonant excitation, $<\tau_{lum}>$ - mean luminescence lifetime. In (b,c), the data for 1 at.% Ho:$LiYF_4$ are added for comparison.

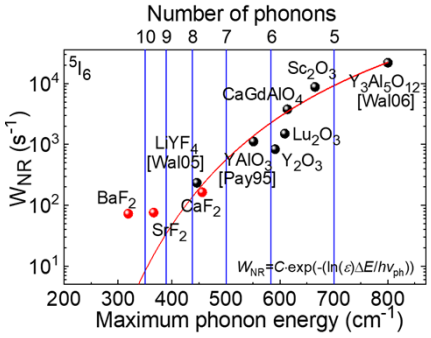


Fig. 11. The relationship between the non-radiative relaxation rate W_{NR} from the $^5I_6$ Ho^{3+} manifold and maximum host phonon energy for different laser materials. *Symbols* – experimental data derived from the luminescence and radiative lifetimes, Eq. (7), *curve* – their fit using Eq. (8), *vertical lines* correspond to *N*-phonon processes.

Optics EXPRESS

Table 6. Evaluation of Multiphonon Non-Radiative Relaxation Rates for Ho^{3+} in Fluoride Crystals[a]

Crystal	State	$\Delta E/h\nu_{ph}$	τ_{rad}, ms	τ_{lum}, ms	η_q	W_{NR}, s^{-1}
Ho:CaF_2	$^5I_5$	5.5	8.42	5.1×10^{-3}	<0.001	1.96×10^5
	$^5I_6$	7.5	7.74	3.41	0.44	164
	$^5I_7$	10.8	16.89	15.21	0.90	6.5
Ho:SrF_2	$^5I_5$	7.0	9.16	8.0×10^{-3}	<0.001	1.25×10^5
	$^5I_6$	9.6	8.13	5.03	0.62	75.8
	$^5I_7$	13.7	17.14	16.91	0.99	0.8
Ho:BaF_2	$^5I_5$	8.0	11.55	17.1×10^{-3}	0.002	0.58×10^5
	$^5I_6$	11.0	9.25	5.53	0.60	72.7
	$^5I_7$	15.8	18.39	18.05	0.98	1.0
Ho:$LiYF_4$	$^5I_6$	7.8	10.57	2.00	0.19	405.4
	$^5I_7$	11.2	17.50	16.61	0.95	3.1

[aa] τ_{rad} – radiative lifetime, τ_{lum} – luminescence lifetime, W_{NR} – probability of non-radiative relaxation.

For the $^5I_7$ state, according to the energy-gap law, the NR relaxation is expected to be weak (as $\Delta E/h\nu_{ph} > 10$ for all three crystals) which is clearly confirmed in our case for all three studied MF_2-type crystals. The luminescence decay is near single exponential, and the τ_{lum} values are relatively long. They tend to increase in the M = Ca → Sr → Ba series, from 15.21 ms to 18.05 ms. This effect is mainly related to the change of the crystal-field strength with the host-forming cations and only to a small extent with the variation of the W_{NR} rate, as expressed by the luminescence quantum efficiencies approaching unity. The long luminescence lifetime of the $^5I_7$ level is beneficial for low-threshold laser operation at ~2 μm. Furthermore, it highlights the suitability of Ho:MF_2 crystals for obtaining high pulse energies from Q-switched lasers.

Owing to the small phonon energies of MF_2 crystals, the $^5I_6$ excited state of Ho^{3+} ions is also weakly affected by the NR relaxation, as $\Delta E/h\nu_{ph} > 7$. As a result, one still observes luminescence lifetimes in the ms-range for this manifold. They also tend to increase in the M = Ca → Sr → Ba series, from 3.41 ms to 5.53 ms, and this variation is now determined by both the change in the radiative transition intensities and the NR relaxation. Indeed, the luminescence quantum efficiency drops to about 1/2. The relatively long lifetime of the $^5I_6$ state indicates the suitability of Ho:MF_2 crystals for 3-μm lasers. The bottleneck effect, $\tau_{lum}(^5I_6) < \tau_{lum}(^5I_7)$, is expected to be overcome by optimizing the rate of ETU from the terminal laser level so as to recycle the electronic population in favor of the $^5I_6$ upper laser manifold.

Finally, for the $^5I_5$ Ho^{3+} level ($\Delta E/h\nu_{ph} > 5$), the effect of NR relaxation on the compositional dependence of the luminescence lifetime becomes dominant, and the measured luminescence lifetimes are in the range of a few μs. We thus conclude that Ho:MF_2 crystals are not suitable for 3.9-μm lasers (at room temperature). Further suppression of the NR relaxation from the $^5I_5$ state is expected to be achieved at cryogenic temperatures.

For the Ho:$LiYF_4$ crystal studied for comparison, the rates of NR relation are higher due to the higher phonon energy, $h\nu_{ph} = 446\,cm^{-1}$. The lifetime of the $^5I_5$ state is less than 1 μs and could not be measured in the present work.

Let us further discuss the effect of the host-dependent phonon properties on the rate of non-radiative relaxation from the $^5I_6$ Ho^{3+} manifold. In Fig. 11, we plot the W_{NR} rate for a number of fluoride and oxide laser host crystals commonly used for Ho doping. The rate of

Optics EXPRESS

multi-phonon non-radiative relaxation is given by [54,55]:

$$W_{NR} = Ce^{-\ln(\varepsilon)\frac{\Delta E}{h\nu_{ph}}}, \tag{10}$$

where C is a constant corresponding to the rate of NR relaxation in the limit of zero energy-gap ($\Delta E \rightarrow 0$), and ε is the ratio between the probabilities of m-phonon and m–1-phonon relaxation. By assuming a constant energy-gap ΔE of 3500 cm^{-1}, and neglecting the host dependence of C and ε material constants, we fitted the available experimental data on W_{NR} with Eq. (8) yielding $C = 1.0 \pm 0.6 \times 10^7$ s^{-1} and $\varepsilon = 4.1 \pm 0.7$. The model explains well the observed evolution of the non-radiative relaxation rate with the maximum phonon energy of the host matrix.

3.6. Error analysis: Ho^{3+} doping inhomogeneity

The error in determining the concentration of active ions (Ho^{3+}, in our case), affects the values of their spectroscopic parameters: i) it directly affects the absorption cross-sections, σ_{abs}, ii) it influences the calculation of radiative transition probabilities via the Judd-Ofelt theory based on the measured absorption spectra (the intrinsic error of this theory is about 20%), and iii) it affects the stimulated-emission cross-sections, σ_{SE}, calculated either by the reciprocity method (based on σ_{abs} spectra) or the F-L formula (via calculated radiative lifetimes and luminescence branching ratios).

In the present work, we used a two-step procedure to control the doping level in the studied samples: first, the segregation coefficient of Ho^{3+} ions, $K_{Ho} = C_{crystal}/C_{melt}$, was determined by the Inductively Coupled Plasma Mass Spectrometry (ICP MS) in "reference" Ho:MF_2 crystals, yielding $K_{Ho} \sim 1$, 0.98 and 0.89 (±0.05) for M = Ca, Sr, and Ba, respectively, for relatively low doping levels about a few at.%. This variation agrees with the ionic radii of VIII-fold fluorine coordinated Ca^{2+} (1.26 Å), Sr^{2+} (1.39 Å), and Ba^{2+} (1.56 Å) compared to that of Ho^{3+} (1.16 Å). Then, the actual doping level in the crystal slices used for spectroscopic measurements was controlled by optical absorption measurements. The relevance of the latter step is dictated by a non-negligible rare-earth dopant distribution across the MF_2 boules grown by the Bridgman technique [56]. The more K_{Ho} differs from unity, the larger is the non-uniform distribution of the ions in the grown crystals.

4. Conclusions

To conclude, fluorite-type crystals MF_2 (M = Ca, Sr, and Ba) doped with Ho^{3+} ions are appealing for lasers and amplifiers operating in the short-wave infrared, at 2 to 3 μm:

i) For the most exploited Ho^{3+} laser transition around 2 μm ($^5I_7 \rightarrow {}^5I_8$), all three crystals benefit from inhomogeneously broadened spectral gain profiles extending far beyond 2 μm thus avoiding the structured water vapor absorption in the air. This is of key importance for broadband tuning of laser emission, and generation and amplification of femtosecond pulses. Ho:CaF_2 provides the largest gain bandwidth of 95 nm potentially supporting sub-100 fs pulses. For mode-locked lasers, the use of Ho:SrF_2 and Ho:BaF_2 could be justified due to their higher nonlinear refractive indices and a stronger Kerr nonlinearity;

ii) We present the first evidence of long-wave multiphonon sidebands of Ho^{3+} ions in MF_2 crystals extending up to at least 2.4 μm which could further contribute to the pulse shortening in mode-locked 2 μm lasers, and enable vibronic lasing at such long wavelengths;

iii) The quantification of electron-phonon interaction allowed us to determine the parameters of energy-transfer upconversion from the $^5I_7$ Ho^{3+} manifold, which is found to be by an order of magnitude weaker than that in the reference Ho:$LiYF_4$ fluoride crystal. This is explained by the lower phonon energies of MF_2 crystals, and weaker transition cross-sections (weaker crystal-field strength);

Optics EXPRESS

iv) Ho:MF_2 crystals also appear promising for 3-µm lasers (the $^5I_6 \rightarrow {}^5I_7$ transition). Due to the decreasing phonon energy in the series M = Ca → Sr → Ba, the Ho:BaF_2 crystals exhibit the longest luminescence lifetime of the $^5I_6$ manifold. On the other hand, Ho:CaF_2 presents stronger spectral line broadening. The demonstration of lasing at 3 µm would require codoping of MF_2 crystals with (Ho^{3+}, Pr^{3+}) for quenching the $^5I_7$ terminal laser level and avoiding the bottleneck effect or (Yb^{3+}, Ho^{3+}) for sensibilization of Ho^{3+} luminescence;

v) Finally, for the 3.9-µm laser transition of Ho^{3+} ($^5I_5 \rightarrow {}^5I_6$), only Ho:$BaF_2$ seems potentially suitable (room-temperature $^5I_5$ lifetime: 18 µs) due to a strong non-radiative relaxation for its Ca and Sr counterparts. Still, cooling to cryogenic temperatures would be required to reduce the NR path. Heavily Ho^{3+}-doping of BaF_2 crystals would potentially prevent the bottleneck effect for this laser transition.

Funding. Agence Nationale de la Recherche (ANR-22-CE08-0031, FLAMIR); Région Normandie (Contrat de plan État-Région (CPER)).

Disclosures. The authors declare no conflicts of interest.

Data availability. Data underlying the results presented in this paper are not publicly available at this time but may be obtained from the authors upon reasonable request.

References

1. A. Schliesser, N. Picqué, and T. W. Hänsch, "Mid-infrared frequency combs," Nat. Photonics **6**(7), 440–449 (2012).
2. J. Ma, Z. Qin, G. Xie, *et al.*, "Review of mid-infrared mode-locked laser sources in the 2.0 µm–3.5 µm spectral region," Appl. Phys. Rev. **6**(2), 021317 (2019).
3. Y. Wang, F. Jobin, S. Duval, *et al.*, "Ultrafast Dy^{3+}:fluoride fiber laser beyond 3 µm," Opt. Lett. **44**(2), 395–398 (2019).
4. M. Pollnau and S. D. Jackson, "Advances in mid-infrared fiber lasers," in *Mid-infrared coherent sources and applications*, M. Ebrahim-Zadeh and I. T. Sorokina, eds. (Springer Netherlands: Dordrecht, 2008), pp. 315–346.
5. I. T. Sorokina, "Crystalline Mid-Infrared Lasers," in *Solid-State Mid-Infrared Laser Sources*, I. T. Sorokina and K. L Vodopyanov, eds. Topics in Applied Physics, vol 89. (Springer, 2003).
6. L. Isaenko, A. Yelisseyev, A. Tkachuk, *et al.*, "New monocrystals with low phonon energy for mid-IR lasers," in *Mid-infrared coherent sources and applications*, M. Ebrahim-Zadeh, I. T. Sorokina, A. Tkachuk, *et al.*, eds. (Springer Netherlands: Dordrecht, 2008), pp. 3–65.
7. E. E. Brown, Z. D. Fleischman, J. McKay, *et al.*, "Ho^{3+} doped low-phonon single crystals and chalcogenide glasses for mid-IR source application," Opt. Mater. Express **13**(5), 1307–1319 (2023).
8. R. S. Quimby and B. G. Aitken, "Multiphonon energy gap law in rare-earth doped chalcogenide glass," J. Non-Cryst. Solids **320**(1-3), 100–112 (2003).
9. E. Brown, Z. Fleischman, J. McKay, *et al.*, "Spectroscopic characterization of low-phonon Er-doped BaF_2 single crystal for mid-IR lasers," Opt. Mater. Express **11**(2), 575–584 (2021).
10. S. Normani, P. Loiko, L. Basyrova, *et al.*, "Mid-infrared emission properties of erbium-doped fluorite-type crystals," Opt. Mater. Express **13**(7), 1836–1851 (2023).
11. X. Zhu and N. Peyghambarian, "High-power ZBLAN glass fiber lasers: Review and prospect," Adv. OptoElectron. **2010**(1), 1–23 (2010).
12. F. Maes, V. Fortin, S. Poulain, *et al.*, "Room-temperature fiber laser at 3.92 µm," Optica **5**(7), 761–764 (2018).
13. K. Eremeev, P. Loiko, A. Benayad, *et al.*, "Efficient continuous-wave Tm,Ho:CaF_2 laser at 2.1 µm," Opt. Lett. **48**(7), 1730–1733 (2023).
14. J. Li, D. D. Hudson, and S. D. Jackson, "High-power diode-pumped fiber laser operating at 3 µm," Opt. Lett. **36**(18), 3642–3644 (2011).
15. R. Stutz, H. C. Miller, K. M. Dinndorf, *et al.*, "High-pulse-energy 3.9-µm lasers in Ho:BYF," Proc. SPIE **5332**, 111–119 (2004).
16. T. Boilard, V. Fortin, M. Lemieux-Tanguay, *et al.*, "1.7 W holmium-doped fluoroindate fiber laser at 3920 nm," Opt. Lett. **49**(10), 2677–2680 (2024).
17. S. D. Jackson, "Mid-infrared holmium fiber lasers," IEEE J. Quantum Electron. **42**(2), 187–191 (2006).
18. B. M. Walsh, N. P. Barnes, M. Petros, *et al.*, "Spectroscopy and modeling of solid state lanthanide lasers: Application to trivalent Tm^{3+} and Ho^{3+} in $YLiF_4$ and $LuLiF_4$," J. Appl. Phys. **95**(7), 3255–3271 (2004).
19. K. A. Pierpoint, M. E. Doroshenko, O. K. Alimov, *et al.*, "Spectroscopic properties of Ho^{3+} optical centers in CaF_2 crystals at the two-micron laser transition," J. Lumin. **228**, 117584 (2020).
20. S. A. Payne, L. L. Chase, L. K. Smith, *et al.*, "Infrared cross-section measurements for crystals doped with Er^{3+}, Tm^{3+}, and Ho^{3+}," IEEE J. Quantum Electron. **28**(11), 2619–2630 (1992).
21. S. Ye, X. Zhou, S. Huang, *et al.*, "Cascade MIR Ho:YLF laser at 2.1 µm and 2.9 µm," Opt. Lett. **47**(21), 5642–5645 (2022).

Optics EXPRESS

22. A.M. Tabirian, H.P. Jenssen, and A. Cassanho, "Efficient, room temperature mid-infrared laser at 3.9 μm in Ho:BaY_2F_8," in *Advanced Solid State Lasers* (Optica Publishing Group, 2001), p. MC5
23. P. Camy, J. L. Doualan, A. Benayad, *et al.*, "Comparative spectroscopic and laser properties of Yb^{3+}-doped CaF_2, SrF_2 and BaF_2 single crystals," Appl. Phys. B **89**(4), 539–542 (2007).
24. F. Druon, S. Ricaud, D. N. Papadopoulos, *et al.*, "On Yb:CaF_2 and Yb:SrF_2: review of spectroscopic and thermal properties and their impact on femtosecond and high power laser performance," Opt. Mater. Express **1**(3), 489–502 (2011).
25. P. Camy, J. L. Doualan, S. Renard, *et al.*, "Tm^{3+}: CaF_2 for 1.9 μm laser operation," Opt. Commun. **236**(4-6), 395–402 (2004).
26. L. Basyrova, P. Loiko, J. L. Doualan, *et al.*, "Thermal lensing, heat loading and power scaling of mid-infrared Er:CaF_2 lasers," Opt. Express **30**(5), 8092–8103 (2022).
27. V. Petit, P. Camy, J.-L. Doualan, *et al.*, "Spectroscopy of Yb^{3+}:CaF_2: from isolated centers to clusters," Phys. Rev. B **78**(8), 085131 (2008).
28. B. Lacroix, C. Genevois, J. L. Doualan, *et al.*, "Direct imaging of rare-earth ion clusters in Yb:CaF_2," Phys. Rev. B **90**(12), 125124 (2014).
29. S. A. Kazanskii and A. I. Ryskin, "Group-III ion clusters in activated fluorite-like crystals," Phys. Solid State **44**(8), 1415–1425 (2002).
30. M. Němec, J. Šulc, M. Jelínek, *et al.*, "Thulium fiber pumped tunable Ho:CaF_2 laser," Opt. Lett. **42**(9), 1852–1855 (2017).
31. J. Liu, C. Zhang, Y. Wang, *et al.*, "Spectral characterization and laser operation of Ho:SrF_2 single-crystal fiber," J. Alloys Compd. **920**, 166009 (2022).
32. K. Veselský, P. Loiko, K. Eremeev, *et al.*, "Broadly tunable continuous-wave Tm,Ho:SrF_2 and Tm,Ho:BaF_2 lasers," Opt. Lett. **49**(19), 5631–5634 (2024).
33. Y. Wang, J. Liu, X. Feng, *et al.*, "~2.9 μm continuous-wavelength laser operation of fiber-pumped Ho, Pr:CaF_2 single crystals," Opt. Mater. **135**, 113329 (2023).
34. J. P. Russell, "The Raman spectrum of calcium fluoride," Proc. Phys. Soc. **85**(1), 194–199-2 (1965).
35. I. Richman, "Longitudinal optical phonons in CaF_2, SrF_2, and BaF_2," J. Chem. Phys. **41**(9), 2836–2837 (1964).
36. E. Cadelano and G. Cappellini, "Electronic structure of fluorides: general trends for ground and excited state properties," Eur. Phys. J. B **81**(1), 115–120 (2011).
37. W. T. Carnall, P. R. Fields, and K. Rajnak, "Electronic energy levels in the trivalent lanthanide aquo ions. I. Pr^{3+}, Nd^{3+}, Pm^{3+}, Sm^{3+}, Dy^{3+}, Ho^{3+}, Er^{3+}, and Tm^{3+}," J. Chem. Phys. **49**(10), 4424–4442 (1968).
38. M. Jelinek, V. Kubeček, W. Ma, *et al.*, "Cryogenic Ho:CaF_2 laser pumped by Tm:fiber laser," Laser Phys. Lett. **13**(6), 065004 (2016).
39. A. A. Kornienko, A. A. Kaminskii, and E. B. Dunina, "Dependence of the line strength of f–f transitions on the manifold energy. II. Analysis of Pr^{3+} in $KPrP_4O_{12}$," Phys. Status Solidi B **157**(1), 267–273 (1990).
40. Z. Pan, P. Loiko, S. Slimi, *et al.*, "Tm,Ho:Ca(Gd,Lu)AlO_4 crystals: Crystal growth, structure refinement and Judd-Ofelt analysis," J. Lumin. **246**, 118828 (2022).
41. H. H. Li, "Refractive index of alkaline earth halides and its wavelength and temperature derivatives," J. Phys. Chem. Ref. Data **9**(1), 161–290 (1980).
42. C. K. Jørgensen and R. Reisfeld, "Judd-Ofelt parameters and chemical bonding," J. Less-Common Met. **93**(1), 107–112 (1983).
43. B. Aull and H. Jenssen, "Vibronic interactions in Nd:YAG resulting in nonreciprocity of absorption and stimulated emission cross sections," IEEE J. Quantum Electron. **18**(5), 925–930 (1982).
44. M. Mujaji, G. D. Jones, and R. W. G. Syme, "Polarization study and crystal-field analysis of the laser-selective excitation spectra of Ho^{3+} ions in CaF_2 and SrF_2 crystals," Phys. Rev. B **46**(22), 14398–14410 (1992).
45. N. Karayianis, D. E. Wortman, and H. P. Jenssen, "Analysis of the optical spectrum of Ho^{3+} in $LiYF_4$," J. Phys. Chem. Solids **37**(7), 675–682 (1976).
46. N. P. Barnes, B. M. Walsh, and E. D. Filer, "Ho:Ho upconversion: applications to Ho lasers," J. Opt. Soc. Am. B **20**(6), 1212–1219 (2003).
47. J. Wang, D. I. Yeom, N. Simakov, *et al.*, "Numerical modeling of in-band pumped Ho-doped silica fiber lasers," J. Lightwave Technol. **36**(24), 5863–5880 (2018).
48. F. Auzel, "Multiphonon orbit-lattice relaxation of excited states of rare-earth ions in crystals," Phys. Rev. B **13**(7), 2809–2817 (1976).
49. A. Braud, S. Girard, J. L. Doualan, *et al.*, "Spectroscopy and fluorescence dynamics of (Tm^{3+}, Tb^{3+}) and (Tm^{3+}, Eu^{3+}) doped $LiYF_4$ single crystals for 1.5-μm laser operation," IEEE J. Quantum Electron. **34**(11), 2246–2255 (1998).
50. A. I. Burshtein, "Hopping mechanism of energy transfer," J. Phys. Chem. Lett. **13**(34), 7972–7979 (2022).
51. S. A. Payne, L. K. Smith, W. L. Kway, *et al.*, "The mechanism of Tm to Ho energy transfer in $LiYF_4$," J. Phys.: Condens. Matter **4**(44), 8525–8542 (1992).
52. S. A. Payne, G. D. Wilke, L. K. Smith, *et al.*, "Auger upconversion losses in Nd-doped laser glasses," Opt. Commun. **111**(3-4), 263–268 (1994).
53. P. Loiko and M. Pollnau, "Stochastic model of energy-transfer processes among rare-earth ions. Example of Al_2O_3:Tm^{3+}," J. Phys. Chem. C **120**(46), 26480–26489 (2016).

Optics EXPRESS

54. M. J. Weber, "Radiative and multiphonon relaxation of rare-earth ions in Y_2O_3," Phys. Rev. **171**(2), 283–291 (1968).
55. C. B. Layne, W. H. Lowdermilk, and M. J. Weber, "Multiphonon relaxation of rare-earth ions in oxide glasses," Phys. Rev. B **16**(1), 10–20 (1977).
56. I. Nicoara, M. Stef, G. Buse, *et al.*, "Growth and characterization of ErF_3 doped BaF_2 crystals," J. Cryst. Growth **547**, 125817 (2020).